Charting the mechanism and reactivity of zirconium oxalate with hydroxamate ligands using density functional theory: implications in new chelate design

Jason P. Holland[1]* and Neil Vasdev[1]

[1] Division of Nuclear Medicine and Molecular Imaging, Massachusetts General Hospital, Department of Radiology, Harvard Medical School, 55 Fruit St., White 427, Boston, Massachusetts, United States of America, 02114

* Corresponding Author:
Dr. Jason P. Holland
Tel: +1-(617)-726-6107
Fax: +1-(617)-726-6165
E-mail: holland.jason@mgh.harvard.edu; jasonpholland@gmail.com

Running Title: *DFT studies on Zr-oxalate reactivity with hydroxamic acids*

One sentence text: *DFT studies on Zr-oxalate reactivity with hydroxamic acids reveals new insight into the mechanism and coordination requirements of $^{89}Zr^{4+}$ ions.*

Abstract

The reaction of $[^{89}Zr(C_2O_4)_4]^{4-}$ with the *tris*-hydroxamate ligand desferrioxamine B (DFO) provides the basis of radiolabelling biological vectors such as antibodies and proteins with the radionuclide ^{89}Zr for positron emission tomography imaging. In this work, density functional theory methods were used to investigate the mechanism of reaction from $[Zr(C_2O_4)_4]^{4-}$ to $Zr(MeAHA)_4$ by ligand substitution with *N*-methyl acetohydroxamate (MeAHA). Calculations were performed under simulated basic and acidic conditions. Ligand substitution under basic conditions was found to be thermodynamically feasible with an overall calculated change in solvation free energy, $\Delta G_{sol} = -97$ kJ mol^{-1} using the B3LYP/DGDZVP methodology and a water continuum solvation model. In contrast, an acid-mediated mechanism of ligand substitution was found to be thermodynamically non-feasible. Molecular orbital analysis provides a rationale for the difference in thermodynamic stability between $[Zr(C_2O_4)_4]^{4-}$ and $Zr(MeAHA)_4$. Overall, the DFT calculations are consistent with observed experimental ^{89}Zr-radiolabelling reactions and suggest that computational methods may prove useful in designing novel chelates for increasing the thermodynamic and kinetic stability of ^{89}Zr-complexes *in vivo*.

Key words: Zirconium, ^{89}Zr, density functional theory, hydroxamates, oxalic acid, DFO, mechanistic studies, ligand design, molecular orbitals.

Introduction

In the fields of radiochemistry and nuclear medicine, there has been tremendous interest and global expansion in the use $^{89}Zr^{4+}$ as a radionuclide (half-life: $t_{1/2} = 78.41$ h, positron yield: $\beta^+ = 22.3\%$) for labelling antibodies for use in immuno-positron emission tomography (Immuno-PET) imaging. Since Perk et al.[1] and Börjesson et al.[2] reported the first clinical studies using ^{89}Zr-radiolabelled antibodies in 2006, more than 24 clinical trials have been initiated across the world in both academia and industry, with at least 11 different ^{89}Zr-based agents currently under evaluation as diagnostic positron emission tomography (PET) radiotracers (source: www.clinicaltrials.gov).

Radiolabelling species with $^{89}Zr^{4+}$ ions typically involves the reaction of the hexadentate, *tris*-hydroxamic acid ligand, Desferrioxamine B (DFO), with a solution of ^{89}Zr-oxalate, $[^{89}Zr(C_2O_4)_4]^{4-}$ at room temperature for 10 minutes to 2 hours.[3] In producing ^{89}Zr-radiolabelled antibodies and other species, the DFO chelate can be attached to the biological vector by using various conjugation methods and linkers.[4] However, the chelate group itself remains unmodified, and in this regard, DFO has emerged as the ligand of choice for ^{89}Zr-radiochemistry.[3, 5-11] While an exact measure of the formation constant of the Zr-DFO complex has yet to be reported, it is likely to exceed that of Fe-DFO (log β = 30.7), and consequently, Zr-DFO has been found to display very high stability *in vivo*. Other chelates have also been investigated for use in complexing $^{89}Zr^{4+}$ ions including polyaminocarboxylate ligands like EDTA and DTPA. However, these alternative chelates have proven to be less stable than DFO for use *in vivo*.[12] Certainly, the quality of ^{89}Zr-mAb images generated from clinical trials supports the supposition that DFO provides an excellent ligand for Zr^{4+} ions. In preclinical studies, catabolism and subsequent release of a (potentially anionic[3]) ^{89}Zr-species has been found to result in modest

accumulation of radioactivity in the bone in murine models.[7-9, 11, 13, 14] It should be noted that whilst bone uptake has not been observed in reported human imaging trials with [89]Zr-DFO-labelled radiotracers, this potential "instability" has, in part, provided the impetus for chemists to begin designing new ligands for [89]Zr chelation that could circumvent potential issues from undesirable irradiation of the marrow.

In 2010, Holland *et al*.[8] noted that Zr-complexes preferentially exhibit high coordination numbers up to 8, and density functional theory (DFT) studies on Zr-DFO revealed that the complex has the capacity to accommodate two additional water molecules as ligands in pseudo-axial and pseudo-equatorial sites. Remarkably, these calculations provide the first piece of data suggesting that water, or likely counter ions such as chloride or acetate *in vivo*, actively coordinate to Zr-DFO ion and in doing so increase the thermodynamic stability of the complex. Unfortunately, a single-crystal X-ray structure of Zr-DFO remains elusive but recent studies by Guérard *et al*.[15] reported the X-ray structure of 8-coordinate Zr(MeAHA)$_4$ – a complex formed between Zr^{4+} ions and 4 ligands of *N*-methyl acetohydroxamato anion.

The work reported here provides a theoretical study on the mechanism of the ligand substitution reaction between $[Zr(C_2O_4)_4]^{4-}$ and *N*-methyl-acetohydroxamic acid (MeAHA), and the nature of the geometric and electronic factors that influence the thermodynamic stability of the Zr(MeAHA)$_4$ complex. It is anticipated that a fundamental understanding of the ligand and coordination requirements for effective complexation of Zr^{4+} ions will aid in the design and synthesis of new chelates, and will facilitate development of the next generation of [89]Zr-radiopharmaceuticals with improved thermodynamic and kinetic stability *in vivo*.

Computational Details

All calculations were conducted using density functional theory (DFT) as implemented in the Gaussian03W Revision B.04 suite of *ab initio* quantum chemistry programs.[16] Normal self-consistent field (SCF) and geometry convergence criteria were employed throughout, and structures were optimised in the gas phase without the use of symmetry constraints. For molecular orbital analysis, the structure of $[Zr(C_2O_4)_4]^{4-}$ was also optimised in D_{2d} symmetry. Harmonic frequency analysis based on analytical second derivative was used to characterise optimised structures as local minima on the potential energy surface. Gas phase geometry optimisations and vibrational frequency calculations were performed by using a variety of exchange-correlation (XC) functionals. The 29 XC functionals investigated can be divided into four categories. (i) Pure GGA functionals (where X = 0) including the first-generation BLYP,[17, 18] BP86,[18-20] BPW91,[18, 21, 22] PW91PW91,[21, 22] and second-generation methods; BPBE,[18, 23] PBEPBE,[23] PBELYP,[17, 23] G96LYP[17, 24] and mPWPW91.[21, 25] (ii) Hybrid-GGA functionals (where X > 0) including the first-generation B1LYP,[17, 18, 26] B3LYP,[17, 18, 27] B3P86,[18-20] B3PW91,[18, 21, 28] BHandH[16, 29] and second-generation methods B97-1,[30, 31] B97-2,[30-32] B98,[30, 33] O3LYP,[17, 34, 35] X3LYP[17, 36] PBE1PBE (also known as PBE0),[23, 37, 38] THCTHH,[39] mPW3LYP (mPWLYP combined with Iop(3/76=1000002000), Iop(3/77=0720008000) and (Iop(3/78=0810010000) keywords),[40] and MPW1N (mPWPW91 and Iop(3/76=0594004060)).[41, 42] (iii) Pure meta-GGA functionals including BB95,[18, 43] BTPSS,[18, 44] TPSSTPSS,[44] and VSXC.[45] (iv) Hybrid meta-GGAs including TPSS1KCIS[44, 46, 47] (TPSSKCIS and (Iop(3/76=0870001300))

and BMK.[48] The origins, nomenclature and characteristics of the XC functionals studied have been described elsewhere.[49-51]

Basis sets evaluated included LANL2DZ[52-55], DGDZVP[56, 57], the Stevens/Basch/Krauss ECP basis sets[58-60] CEP-4G, CEP-31G, CEP-121G; SDDALL[52] (with default effective core potentials applied for all atoms with atomic number, $Z > 2$). Mixed basis set combinations were employed by evoking user-defined basis sets with the "gen" keyword. In all cases, mixed basis set combinations employed the all-electron 6-31+G(d) basis set[61, 62] for all ligand atoms with LANL2DZ (using the default LANL effective core potential for Zr), or the all-electron double-ζ "Sapporo-DZP" or triple-ζ "Sapporo-TZP" basis sets by Noro *et al.*[63]

The effects of solvation were incorporated[64, 65] iteratively by performing self-consistent reaction field (SCRF) calculations using the integral equation formalism polarisable continuum model (IEFPCM) initially developed by Tomasi and co-workers.[66] Due to limitations in computational capacity, full geometry optimisations in the presence of the solvent field were beyond our capacity. Therefore, we used the optimised gas phase geometries as input structures for static, single point calculations incorporating the solvent reaction field. The solute-solvent boundary was defined by using a solvent excluding surface (SES).[67] The molecular solute surface was defined by using the United Atom Topological model (UAHF) for the radii of the solute atoms.[26] We used a water solvent continuum model with dielectric constant, $\varepsilon = 78.39$, and solvent sphere radius, $R_{solv} = 1.385$ Å. The choice of solvation model reflects our standard aqueous phase conditions employed in the radiochemical synthesis of many [89]Zr-based radiotracers for positron emission tomography (PET).[3, 8, 9, 11, 13, 68-73] Optimised structures and molecular orbitals were analysed by using Chemcraft (version 1.7, build 365).

Results and Discussion

Methodology selection

Prior to commencing mechanistic studies using density functional theory (DFT) methods on the ligand substitution reaction between $[Zr(C_2O_4)_4]^{4-}$ and *N*-methyl-acetohydroxamic acid, we evaluated the use of different basis sets and XC functionals for their ability to provide an accurate representation of the electron structure of this class of complexes. Initially, 9 different basis set combinations were used in combination with the B3LYP exchange-correlation functionals to identify a basis set that could provide a balance between computational accuracy compared to the experiment and computational efficiency (Table 1). Geometric parameters compared include the bond lengths (in Å), r(Zr-ON), r(Zr-OC), r(N-C), r(N-CH_3), and r(C-CH_3) as well as the overall weighted root-mean-squared-deviation (RMSD / Å; weighted to the atomic masses of all heavy atoms, i.e. excluding hydrogen). The calculations revealed asymmetry in the optimised structures of Zr(MeAHA)$_4$ consistent with two distinct MeAHA ligand environments (Figure 1). MeAHA ligands *trans* to each other were found to be equivalent. This asymmetry is consistent with the experimental X-ray data which showed a range in r(Zr-ON) and r(Zr-OC) bond lengths from 2.140 – 2.228 Å and 2.182 – 2.206 Å, respectively. As noted by Guérard *et al.*,[15] inequivalence of MeAHA ligands in the X-ray structure is in part due to rapid exchange of ligands between different coordination geometries (calculated to be a barrierless intramolecular geometrical interconversion between e.g. dodecahedral and square antiprism 8-coordinate structures, and therefore, fluxional on the NMR time scale[74]), and also influenced by disorder in the experimental X-ray data leading to potential discrepancies in the assignments of N and C atoms. Nevertheless, assessment of the structural parameters and overall RMSD showed that whilst use of the all electron Sapporo-TZP/6-31+G(d) basis set gave the smallest heavy atom

weighted RMSD of 0.282 Å, this basis set required 565 basis functions and tended to slightly underestimate the average $r(Zr-\underline{O}N)$ bond length by 0.021 Å and overestimate the average $r(Zr-\underline{O}C)$ bond length by 0.032 Å. Comparison between the optimised structures calculated by using LANL2DZ or the mixed basis LANL2DZ/6-31+G(d) showed that a larger, all electron basis set, particularly for the MeAHA ligands, provided a more accurate structure with RMSD values of 0.377 Å and 0.292 Å, respectively. Overall, the DGDZVP (requiring the use of 420 basis functions) provided a suitable balance between structural accuracy (RMSD = 0.287 Å) and computational efficiency. Therefore, subsequent calculations employed the DGDZVP basis set.

Next we evaluated the accuracy of various XC functionals. In total, 29 XC functionals, spanning first- and second-generation pure and hybrid generalised gradient approximation (GGA) DFT methods, through to more recent pure and hybrid meta-GGA methods were evaluated by optimising the structure of $Zr(MeAHA)_4$ *in vacuo* and comparing the calculated structures to the averaged experimental single-crystal X-ray structure (Table 2).[15] As anticipated, the pure DFT methods provided a reasonable estimation of the $Zr(MeAHA)_4$ geometry with overall RMSD values ranging from 0.231 Å for PBEPBE to 0.244 Å for G96LYP. However, comparison of the crucial Zr-O bond lengths showed that while use of pure DFT methods improved the geometry of the ligands, this occurs at the expense of elongating the average $r(Zr-\underline{O}N)$ and $r(Zr-\underline{O}C)$ bond lengths. Hybrid-GGA methods are well-known to provide more accurate energetics, and thus, are more suitable for computational mechanistic studies requiring comparison of thermodynamic properties. Here, we found that the hybrid-GGA methods provided slightly poorer overall RMSD values than pure methods, ranging from 0.240 Å for O3LYP to 0.315 Å for BHandH. However, average Zr-O bond lengths improved with a minor error introduced in the MeAHA ligand geometries. In conclusion, only minor differences were

observed in the optimised geometries of Zr(MeAHA)$_4$ between different XC functionals with no method appearing to stand out as superior. On this basis, subsequent calculations on the reaction pathway for ligand substitution were completed using the B3LYP/DGDZVP methodology. For comparison, and to expedite the calculations, we also employed the B3LYP/LANL2DZ methodology for initial optimisations of all structures.

Ligand substitution under basic conditions

Whilst the standard protocol proposed by Vosjan *et al.*[14] involves [89]Zr-radiolabeling in a 0.5 M HEPES buffer at pH 7.1 – 7.3, in our experience, the reaction between [^{89}Zr(C$_2$O$_4$)$_4$]$^{4-}$ and DFO has been shown to proceed rapidly and efficiently over a wide pH window from 6 to 9.5.[3, 8] The limiting factor is not the radiolabeling chemistry but rather the stability or solubility of the biological vector (most frequently an antibody) toward extremes of basic pH (JPH – unpublished data and Reference[3]). The fact that [^{89}Zr(C$_2$O$_4$)$_4$]$^{4-}$ remains stable in aqueous solution, and resistant to aggregation, precipitation and/or hydrolysis is remarkable given the facile and rapid ligand exchange reaction with hydroxamates like DFO. To shed light on this reaction, our calculations focused on the step-wise ligand replacement from [Zr(C$_2$O$_4$)$_4$]$^{4-}$ to give Zr(MeAHA)$_4$ *via* a dissociative pathway involving 6-coordinate, octahedral Zr-species (Scheme 1). Various geometric isomers are possible for the different Zr-species. Therefore, to elucidate the most energetically favourable pathway we optimised the structures of all isomers (data not shown). Given that ligand exchange and isomerisation reactions are expected to be rapid under experimental conditions,[8, 10, 15] only the species with the lowest standard free energy in water solvent, G_{sol} / kJ mol^{-1}, are presented.

The first pathway investigated modelled the experimental situation for [89]Zr-radiolabelling of DFO under simulated basic conditions (Figure 2). The starting material $[Zr(C_2O_4)_4]^{4-}$ can be converted to $Zr(MeAHA)_4$ and 4 mole equivalents of dibasic oxalate $(C_2O_4^{2-})$ anions using fully deprotonated hydroxamate MeAHA in 8 sequential steps (4 separate oxalate dissociation-hydroxamate addition reactions). The reaction coordinate revealed that each of the four sequential oxalate dissociation steps involves a comparable increase free energy to give the 6-coordinate octahedral intermediates. The B3LYP/DGDZVP calculated differences in free energy between the 8-coordinate species $[Zr(C_2O_4)_4]^{4-}$, $[Zr(C_2O_4)_3(MeAHA)]^{3-}$, $[Zr(C_2O_4)_2(MeAHA)_2]^{2-}$, and $[Zr(C_2O_4)(MeAHA)_3]^{-}$, and their corresponding 6-coordinate intermediates $[Zr(C_2O_4)_3]^{2-}$, $[Zr(C_2O_4)_2(MeAHA)]^{-}$, $Zr(C_2O_4)(MeAHA)_2$, and $[Zr(MeAHA)_3]^{+}$ were found to be 146, 143, 160 and 143 kJ mol^{-1}, respectively. Interestingly, a similar trend was observed using the B3LYP/LANL2DZ methodology. Equivalent energetic differences of 170, 166, 179 and 183 kJ mol^{-1} were found indicating that, in spite of the reduced structural accuracy of the LANL2DZ calculations *versus* the DGDZVP, similar chemical conclusions emerge. Each oxalate to hydroxamate ligand substitution reaction is calculated to be thermodynamically feasible (ΔG_{sol} <0 kJ mol^{-1}) with the final step, $[Zr(MeAHA)_3]^{+}$ to $Zr(MeAHA)_4$ being the most favourable with a change in free energy ΔG_{sol} = –58 kJ mol^{-1} (DGDZVP). Overall, the ligand substitution reaction of $[Zr(C_2O_4)_4]^{4-}$ and 4 MeAHA anions to give $Zr(MeAHA)_4$ plus 4 equivalents of $C_2O_4^{2-}$ is calculated to be thermodynamically feasible with ΔG_{sol} = –97 kJ mol^{-1} (DGDZVP).

It is interesting to note that in the 8-coordinate Zr-species (Scheme 1 and Figure 2), the frontier molecular orbital energy gap (Δ_{FMO} / eV) shows a steady increase upon step-wise ligand substitution of oxalate to MeAHA from 4.933 eV in $[Zr(C_2O_4)_4]^{4-}$, to 5.219 eV in $Zr(MeAHA)_4$. Importantly, this increase in Δ_{FMO} mirrors the change in ΔG_{sol}, indicating the potential value of

using relative differences in DFT calculated frontier orbital energy gaps as a tool for predicting

the thermodynamic stability of Zr species derived from novel hydroxamate-based ligands. In

spite of the changes calculated in ΔG_{sol} and Δ_{FMO}, virtually no change was observed in the

calculated Mulliken charge (range: $1.31e$ to $1.61e$) or Natural Population Analysis charge (range:

$2.56e$ to $2.71e$) on the Zr ion. In contrast to calculated ΔG_{sol} and Δ_{FMO} values, charge analysis

appears less useful in the future computational design of new ligands for chelating $^{89}Zr^{4+}$ ions.

Similarly, changes in r(Zr-O) bond lengths were found to provide a poor correlation with ΔG_{sol}

and Δ_{FMO} (data not shown) and are likely to be less useful in designing new ligands for Zr. We

also note that due to the change in overall charge on ligand substitution, and the dominance of

electrostatic interactions in solvation of these species, inclusion of the water continuum model

was found to be essential for calculation of the energetics of these Zr-species.

Ligand substitution under acidic conditions

Experiments have shown that the reaction between $[Zr(C_2O_4)_4]^{4-}$ and DFO is spontaneous under

neutral or even slightly acidic pH around 6.[3, 8, 14, 15] To investigate a potential role of a proton-

mediated mechanism of ligand substitution in the synthesis of Zr(MeAHA)$_4$, we calculated the

reaction pathway under simulated "acidic" conditions (noted as an approximation to pH <4).

Prior to calculating the protonated Zr-species, the energetics of proton transfer between

MeAHA and oxalic acid were investigated (Scheme 2) using the B3LYP/DGDZVP

methodology. As noted by Dean,[75] the most stable conformer of the oxalate dianion is the D_{2d}

geometry with a long r(C-C) bond and a 90° dihedral twist about this bond. In this work, the D_{2d}

conformer was found to be ~15 kJ mol^{-1} more stable than the planar D_{2h} conformer. The

calculations revealed that in water, disproportionation of two moles of monobasic $HC_2O_4^-$ to give

$C_2O_4^{2-}$ and oxalic acid ($H_2C_2O_4$) is unfavourable with ΔG_{sol} = +53 kJ mol^{-1} (Scheme 2, Reaction 1). Thus, in the simulated acidic conditions used in these calculations (i.e. when a proton is released from the addition of MeAHA to the Zr-species), $HC_2O_4^-$ will exist in solution. Calculation of the energetics of geometric isomerisation of MeAHA revealed that the sterically less hindered E isomer is favoured by 12 kJ mol^{-1} for the MeAHA conjugate base, and by 8 kJ mol^{-1} for the MeAHA acid (Scheme 2, Reactions 2 and 3, respectively). Thus, as anticipated, addition of MeAHA anion to a Zr-species involves a small energy requirement associated with ligand isomerisation to the coordinating Z isomer. The calculations also faithfully reproduced the expected protic equilibria between MeAHA acid and mono- and dibasic oxalate anions (Scheme 2, Reactions 4 and 5) indicating that the weaker acid MeAHA will remain protonated in the presence of $H_2C_2O_4$ or $HC_2O_4^-$. These calculated data are consistent with the known pK_a values of MeAHA[76] (8.75), $H_2C_2O_4$ (1.25) and $HC_2O_4^-$ (4.14).

The DFT calculated acid-mediated reaction pathway for ligand exchange is presented in Scheme 3 and Figure 3. The most prominent conclusion arising from these calculations is that whilst protonation of the oxalate ligands on various Zr-species results in an intermediate of slightly lower energy than the 6-coordinate species, overall, the acid-mediated pathway is thermodynamically non-feasible in the absence of a suitable base. The change in relative solvated free energy from $[Zr(C_2O_4)_4]^{4-}$ and 4 equivalents of MeAHA acid, to Zr(MeAHA)$_4$ plus 4 equivalents of the more stable monobasic $HC_2O_4^-$ was calculated to be +92 kJ mol^{-1} (DGDZVP). We note that the non-feasibility of this acid-mediated pathway would not be circumvented by changing the starting material from [89]Zr-oxalate to, for example, [89]Zr-chloride.[3] Rather, addition of a more powerful base than $C_2O_4^{2-}$ (or chloride anions) in water is required. These calculations are consistent with the fact that the majority of [89]Zr radiochemical reactions

require the use of Na_2CO_3 to neutralise the excess oxalic acid. Experimentally, the carbonate anions act as a proton-acceptor, driving the [89]Zr-radiolabelling reactions toward the various [89]Zr-hydroxamate species *via* a reaction pathway akin to "basic" mechanism shown in Figure 3. In this regard, the DFT calculations are fully consistent with experimental [89]Zr-radiolabelling reactions.

Molecular orbital analysis of $[Zr(C_2O_4)_4]^{4-}$ *and* $Zr(MeAHA)_4$

Molecular orbital (MO) analyses of $[Zr(C_2O_4)_4]^{4-}$ (dodecahedral structure with D_{2d} symmetry) and $Zr(MeAHA)_4$ (distorted dodecahedral geometry in C_1 symmetry) are presented in Figures 4 and 5, respectively. In the electronic structures of both $[Zr(C_2O_4)_4]^{4-}$ and $Zr(MeAHA)_4$, the MO coefficient characterising the metal d orbital contribution to several of the highest occupied orbitals molecular orbitals (HOMOs) in the occupied manifold is relatively minor. In contrast, the metal d orbital component of several of the lowest unoccupied molecular orbitals (LUMOs) is large, consistent with the d^0 configuration of the Zr^{4+} ion. The calculated Mulliken and NPA charges on the Zr ion in $[Zr(C_2O_4)_4]^{4-}$ are $1.43e$ and $2.71e$, and for $Zr(MeAHA)_4$ are $1.31e$ and $2.61e$, respectively. This decrease in positive charge from purely ionic Zr^{4+} is consistent with the anticipated donation of electron density from the donor oxygen atoms to the metal ion. The MO analysis revealed that the principal metal ion d orbitals involved in accepting ligand electron density are the xy (HOMO-17) and x^2-y^2 (HOMO-19 and HOMO-23) orbitals in $[Zr(C_2O_4)_4]^{4-}$.

Due to the lack of symmetry in the calculated structure of $Zr(MeAHA)_4$, a change in the standard orientation of the Cartesian axes compared to $[Zr(C_2O_4)_4]^{4-}$, and also due to the twisting of the ligands in the pseudo-dodecahedral geometry, heavy d orbital mixing is evident in the MOs of $Zr(MeAHA)_4$. This d orbital mixing complicates MO analysis. In $Zr(MeAHA)_4$, mixing

of the xy, xz, yz and z^2 orbitals appears to increase the degree of overlap between these hybrid metal orbitals and several of the ligand-based $p\sigma$ donor orbitals on the oxygen atoms (HOMO-7, 8, 9 and 11). The x^2-y^2 remains bonding (HOMO-3) but is raised in energy in comparison to the equivalent orbital identified in $[Zr(C_2O_4)_4]^{4-}$ (B1-symmetry, $p\pi$-bonding, HOMO-17). On balance, the increased overlap in the mixed d orbitals for $Zr(MeAHA)_4$, and consequent increased overlap with ligand-based donor oxygen orbitals causes a slight, yet important increase in the "covalent-character" of the complex. Increased covalent-character arising from more polarised electron density in the MeAHA ligand (with higher negative charge located on the NO oxygen atoms compared to the carbonyl group) and increased electron density donation to the metal ion results in the larger Δ_{FMO} energy gap, and an increase in the thermodynamic stabilisation of $Zr(MeAHA)_4$ *versus* $[Zr(C_2O_4)_4]^{4-}$.

The MO analysis suggests that if polarisation of charge density between the NO and carbonyl oxygen (CO) donor atoms in the didentate hydroxamate donor moiety can be increased by modifying the electronics of the backbone (methyl group) substituents, the ligand-to-metal orbital overlap and electron donation may be increased, leading to a potential further increase in the thermodynamic stability of the Zr complex.

Future design and synthesis of ligands for coordinating $^{89}Zr^{4+}$ ions

Based on these calculations, it is conceivable that a design strategy toward synthesising new *poly*-hydroxamic acid ligands with increased stabilisation of $^{89}Zr^{4+}$ ions should aim to include: 1) addition of a 4th hydroxamic acid group to generate 8-coordinate species, 2) increased ligand flexibility, whilst maintaining preorganisation, to accommodate the increased size of the first coordination sphere from the addition of 2 donor atoms (from 6- to 8-coordinate), and 3)

modification of the ligand electronics to increase the acidity/donor capabilities of the hydroxamic acid groups, potentially increasing the magnitude of "covalent-character" bonding between the ligand and $^{89}Zr^{4+}$ ions. Increasing the denticity of a *poly*-hydroxamate ligand from 6 (as in DFO) to 8 will have the added benefit of increasing the energy stabilisation attained from increasing the magnitude of the chelate effect. In addition, DFT calculations are useful in "predicting" the thermodynamic stability of potential Zr-complexes with new ligands by calculating either full reaction pathway energetics in terms of ΔG_{sol} / kJ mol^{-1}, or equally, using standalone calculations comparing the magnitude of the frontier molecular orbital energy gap, Δ_{FMO} / eV.

Conclusion

DFT calculations provide a rationale for the mechanism of sequential dissociation-addition ligand substitution reactions in ^{89}Zr-radiochemical reactions. The calculations reveal that step-wise oxalate-dissociate followed by addition of the hydroxamate ligand MeAHA under simulated basic conditions is thermodynamically feasible, leading to the rapid and spontaneous conversion of $[Zr(C_2O_4)_4]^{4-}$ to $Zr(MeAHA)_4$. These calculations are fully consistent with observed experimental reactions and suggest that DFT may provide a useful tool in designing the next generation of *poly*-dentate hydroxamate ligands for increasing the thermodynamic and kinetic stability of new ^{89}Zr-radiolabelled species *in vivo*.

Acknowledgements

References

1. L. R. Perk, O. J. Visser, M. Stigter-van Walsum, M. J. W. D. Vosjan, G. W. M. Visser, J. M. Zijlstra, P. C. Huijgens and G. A. M. S. van Dongen, *European Journal of Nuclear Medicine and Molecular Imaging*, 2006, **33**, 1337-1345.
2. P. K. E. Börjesson, Y. W. S. Jauw, R. Boellaard, R. de Bree, E. F. I. Comans, J. C. Roos, J. A. Castelijns, M. J. W. D. Vosjan, J. A. Kummer, C. R. Leemans, A. A. Lammertsma and G. A. M. S. van Dongen, *Clin Cancer Res*, 2006, **12**, 2133-2140.
3. J. P. Holland, Y. Sheh and J. S. Lewis, *Nuclear medicine and biology*, 2009, **36**, 729-739.
4. M. A. Deri, B. M. Zeglis, L. C. Francesconi and J. S. Lewis, *Nuclear medicine and biology*, 2013, **40**, 3-14.
5. W. E. Meijs, J. D. M. Herscheid, H. J. Haisma and H. M. Pinedo, *Appl. Radiat. Isot.*, 1992, **43**, 1443-1447.
6. W. E. Meijs, H. J. Haisma, R. Van der Schors, R. Wijbrandts, K. Van den Oever, R. P. Klok, H. M. Pinedo and J. D. M. Herscheid, *Nuc Med Biol*, 1996, **23**, 439-448.
7. I. Verel, G. W. M. Visser, R. Boellaard, M. Stigter-van Walsum, G. B. Snow and G. A. M. S. van Dongen, *J. Nucl Med*, 2003, **44**, 1271-1281.
8. J. P. Holland, V. Divilov, N. H. Bander, P. M. Smith-Jones, S. M. Larson and J. S. Lewis, *Journal of nuclear medicine : official publication, Society of Nuclear Medicine*, 2010, **51**, 1293-1300.
9. J. P. Holland, E. Caldas-Lopes, V. Divilov, V. A. Longo, T. Taldone, D. Zatorska, G. Chiosis and J. S. Lewis, *PloS one*, 2010, **5**, e8859.
10. J. P. Holland and S. Lewis Jason, *Technetium and Other Radiometals in Chemistry and Medicine, Eds: Ulderico Mazzi, William C. Eckelman, Wynn A. Volkert, Publisher: Servizi Grafici Editoriali snc, Padova, Italy*, 2010, 187-192.
11. J. P. Holland, M. J. Evans, S. L. Rice, J. Wongvipat, C. L. Sawyers and J. S. Lewis, *Nature medicine*, 2012, **18**, 1586-1591.
12. T. J. Wadas, E. H. Wong, G. R. Weisman and C. J. Anderson, *Chemical Reviews*, 2010, **110**, 2858-2902.
13. J. P. Holland, G. Normand, A. Ruggiero, J. S. Lewis and J. Grimm, *Molecular imaging*, 2011, **10**, 177-186, 171-173.
14. M. J. W. D. Vosjan, L. R. Perk, G. W. M. Visser, M. Budde, P. Jurek, G. E. Kiefer and G. A. M. S. van Dongen, *Nat. Protocols*, 2010, **5**, 739-743.
15. F. Guerard, Y. S. Lee, R. Tripier, L. P. Szajek, J. R. Deschamps and M. W. Brechbiel, *Chemical communications*, 2013, **49**, 1002-1004.
16. R. B. Gaussian 03W, M. J. Frisch, G. W. Trucks, H. B. Schlegel, G. E. Scuseria, , J. R. C. M. A. Robb, J. A. Montgomery, Jr., T. Vreven, , J. C. B. K. N. Kudin, J. M. Millam, S. S. Iyengar, J. Tomasi, , B. M. V. Barone, M. Cossi, G. Scalmani, N. Rega, , H. N. G. A. Petersson, M. Hada, M. Ehara, K. Toyota, , J. H. R. Fukuda, M. Ishida, T. Nakajima, Y. Honda, O. Kitao, , M. K. H. Nakai, X. Li, J. E. Knox, H. P. Hratchian, J. B. Cross, , J. J. C. Adamo, R. Gomperts, R. E. Stratmann, O. Yazyev, , R. C. A. J. Austin, C. Pomelli, J. W. Ochterski, P. Y. Ayala, , G. A. V. K. Morokuma, P. Salvador, J. J. Dannenberg, , S. D. V. G. Zakrzewski, A. D. Daniels, M. C. Strain, , D. K. M. O. Farkas, A. D. Rabuck, K. Raghavachari, , J. V. O. J. B. Foresman, Q. Cui, A. G. Baboul, S. Clifford, , B. B. S. J. Cioslowski, G. Liu, A. Liashenko, P. Piskorz, , R. L. M. I. Komaromi, D. J. Fox, T. Keith, M. A. Al-Laham, , A. N. C. Y. Peng, M. Challacombe, P. M. W. Gill, , W. C. B.

Johnson, M. W. Wong, C. Gonzalez, and J. A. Pople, and I. Gaussian, Pittsburgh PA, 2003., 2003.

17.   C. Lee, W. Yang and R. G. Parr, *Physical Review B: Condensed Matter and Materials Physics*, 1988, **37**, 785-789.

18.   A. D. Becke, *Physical Review A: Atomic, Molecular, and Optical Physics*, 1988, **38**, 3098-3100.

19.   J. P. Perdew, *Physical Review B: Condensed Matter and Materials Physics*, 1986, **33**, 8800.

20.   J. P. Perdew, *Phys. Rev. B: Condens. Matter*, 1986, **33**, 8822.

21.   J. P. Perdew, *Electronic structure of solids '91*, 1991, 11.

22.   K. Burke, J. P. Perdew and Y. Wang, *Electron density functional theory*, 1998, 81.

23.   J. P. Perdew, K. Burke and M. Ernzerhof, *Phys. Rev. Lett.*, 1996, **77**, 3865-3868.

24.   P. M. W. Gill, *Mol. Phys.*, 1996, **89**, 433.

25.   C. Adamo and V. Barone, *J. Chem. Phys.*, 1998, **108**, 664-675.

26.   C. Adamo and V. Barone, *Chem. Phys. Lett.*, 1997, **274**, 242-250.

27.   P. J. Stephens, F. J. Devlin, C. F. Chabalowski and M. J. Frisch, *Journal of Physical Chemistry*, 1994, **98**, 11623-11627.

28.   A. D. Becke, *Journal of Chemical Physics*, 1993, **98**, 5648-5652.

29.   A. D. Becke, *J. Chem. Phys.*, 1993, **98**, 1372-1377.

30.   A. D. Becke, *J. Chem. Phys.*, 1997, **107**, 8554-8560.

31.   F. A. Hamprecht, A. J. Cohen, D. J. Tozer and N. C. Handy, *J. Chem. Phys.*, 1998, **109**, 6264-6271.

32.   P. J. Wilson, T. J. Bradley and D. J. Tozer, *J. Chem. Phys.*, 2001, **115**, 9233-9242.

33.   H. L. Schmider and A. D. Becke, *J. Chem. Phys.*, 1998, **108**, 9624-9631.

34.   N. C. Handy and A. J. Cohen, *Mol. Phys.*, 2001, **99**, 403-412.

35.   W. M. Hoe, A. J. Cohen and N. C. Handy, *Chem. Phys. Lett.*, 2001, **341**, 319-328.

36.   X. Xu and A. Goddard William, 3rd, *Proc Natl Acad Sci U S A*, 2004, **101**, 2673-2677.

37.   C. Adamo, M. Cossi and V. Barone, *Theochem*, 1999, **493**, 145-157.

38.   J. P. Perdew, K. Burke and Y. Wang, *Phys. Rev. B: Condens. Matter*, 1996, **54**, 16533-16539.

39.   A. D. Boese and N. C. Handy, *J. Chem. Phys.*, 2002, **116**, 9559-9569.

40.   Y. Zhao and D. G. Truhlar, *J. Phys. Chem. A*, 2004, **108**, 6908-6918.

41.   B. J. Lynch, Y. Zhao and D. G. Truhlar, *J. Phys. Chem. A*, 2003, **107**, 1384-1388.

42.   B. L. Kormos and C. J. Cramer, *J. Phys. Org. Chem.*, 2002, **15**, 712-720.

43.   A. D. Becke, *J. Chem. Phys.*, 1996, **104**, 1040-1046.

44.   J. Tao, J. P. Perdew, V. N. Staroverov and G. E. Scuseria, *Phys. Rev. Lett.*, 2003, **91**, 146401/146401-146401/146404.

45.   T. Van Voorhis and G. E. Scuseria, *J. Chem. Phys.*, 1998, **109**, 400-410.

46.   J. B. Krieger, J. Chen and G. J. Iafrate, *Electron correlations and materials properties*, 1999, 463.

47.   Y. Zhao and D. G. Truhlar, *Phys. Chem. Chem. Phys.*, 2005, **7**, 2701-2705.

48.   A. D. Boese and J. M. L. Martin, *J. Chem. Phys.*, 2004, **121**, 3405-3416.

49.   M. M. Quintal, A. Karton, M. A. Iron, A. D. Boese and J. M. L. Martin, *J Phys Chem A*, 2006, **110**, 709-716.

50.   Y. Zhao, J. Pu, B. J. Lynch and D. G. Truhlar, *Phys. Chem. Chem. Phys.*, 2004, **6**, 673-676.

51.   J. P. Holland and J. C. Green, *Journal of computational chemistry*, 2010, **31**, 1008-1014.
52.   T. H. J. Dunning and P. J. Hay, *Ed. H. F. Schaefer III, Vol. 3 (Plenum, New York) 1-28.*, 1976, **3**, 1-28.
53.   P. J. Hay and W. R. Wadt, *The Journal of Chemical Physics*, 1985, **82**, 299-310.
54.   P. J. Hay and W. R. Wadt, *The Journal of Chemical Physics*, 1985, **82**, 270-283.
55.   W. R. Wadt and P. J. Hay, *The Journal of Chemical Physics*, 1985, **82**, 284-298.
56.   N. Godbout, D. R. Salahub, J. Andzelm and E. Wimmer, *Canadian Journal of Chemistry*, 1992, **70**, 560-571.
57.   C. Sosa, J. Andzelm, B. C. Elkin, E. Wimmer, K. D. Dobbs and D. A. Dixon, *The Journal of Physical Chemistry*, 1992, **96**, 6630-6636.
58.   W. J. Stevens, H. Basch and M. Krauss, *The Journal of Chemical Physics*, 1984, **81**, 6026-6033.
59.   W. J. Stevens, M. Krauss, H. Basch and P. G. Jasien, *Canadian Journal of Chemistry*, 1992, **70**, 612-630.
60.   T. R. Cundari and W. J. Stevens, *The Journal of Chemical Physics*, 1993, **98**, 5555-5565.
61.   V. A. Rassolov, J. A. Pople, M. A. Ratner and T. L. Windus, *Journal of Chemical Physics*, 1998, **109**, 1223-1229.
62.   V. A. Rassolov, M. A. Ratner, J. A. Pople, P. C. Redfern and L. A. Curtiss, *Journal of computational chemistry*, 2001, **22**, 976-984.
63.   T. Noro, M. Sekiya and T. Koga, *Theor Chem Acc*, 2012, **131**, 1-8.
64.   R. J. Hall, M. M. Davidson, N. A. Burton and I. H. Hillier, *Journal of Physical Chemistry*, 1995, **99**, 921-924.
65.   J. L. Chen, L. Noodleman, D. A. Case and D. Bashford, *Journal of Physical Chemistry*, 1994, **98**, 11059-11068.
66.   J. Tomasi, B. Mennucci and R. Cammi, *Chemical Reviews (Washington, DC, United States)*, 2005, **105(8)**, 2999-3094.
67.   M. L. Connolly, *Science (Washington, DC, United States)*, 1983, **221**, 709-713.
68.   A. Ruggiero, J. P. Holland, T. Hudolin, L. Shenker, A. Koulova, N. H. Bander, J. S. Lewis and J. Grimm, *Journal of nuclear medicine : official publication, Society of Nuclear Medicine*, 2011, **52**, 1608-1615.
69.   A. Ruggiero, J. P. Holland, J. S. Lewis and J. Grimm, *Journal of nuclear medicine : official publication, Society of Nuclear Medicine*, 2010, **51**, 1123-1130.
70.   A. Ruggiero, C. H. Villa, J. P. Holland, S. R. Sprinkle, C. May, J. S. Lewis, D. A. Scheinberg and M. R. McDevitt, *International journal of nanomedicine*, 2010, **5**, 783-802.
71.   C. Heneweer, J. P. Holland, V. Divilov, S. Carlin and J. S. Lewis, *Journal of nuclear medicine : official publication, Society of Nuclear Medicine*, 2011, **52**, 625-633.
72.   D. Ulmert, M. J. Evans, J. P. Holland, S. L. Rice, J. Wongvipat, K. Pettersson, P. A. Abrahamsson, P. T. Scardino, S. M. Larson, H. Lilja, J. S. Lewis and C. L. Sawyers, *Cancer discovery*, 2012, **2**, 320-327.
73.   M. J. Evans, J. P. Holland, S. L. Rice, M. G. Doran, S. M. Cheal, C. Campos, S. D. Carlin, I. K. Mellinghoff, C. L. Sawyers and J. S. Lewis, *Journal of Nuclear Medicine*, 2013, **54**, 90-95.
74.   J. K. Burdett, R. Hoffmann and R. C. Fay, *Inorganic chemistry*, 1978, **17**, 2553-2568.
75.   P. A. W. Dean, *Journal of Chemical Education*, 2011, **89**, 417-418.
76.   R. Codd, *Coordination Chemistry Reviews*, 2008, **252**, 1387-1408.

Figure and Table Legends

Figure 1. Schematic representation of the optimised geometry of Zr(MeAHA)$_4$ and atom numbering scheme used in Tables 1 and 2.

Table 1. Comparison of selected geometric parameters from the DFT optimised structure of Zr(MeAHA)$_4$ in gas phase, C_1-symmetry using the B3LYP exchange-correlation functional and different basis sets (see Computational Details section for full details).

Table 2. Comparison of selected geometric parameters from the DFT optimised structure of Zr(MeAHA)$_4$ in gas phase, C_1-symmetry using different XC functionals in combination with the DGDZVP basis set (see Computational Details section for full details).

Scheme 1. Reaction scheme showing the 8-step, sequential oxalate dissociation – hydroxamate addition ligand substitution reaction converting the starting material $[Zr(C_2O_4)_4]^{4-}$ into the Zr(MeAHA)$_4$ product. This reaction models the experimental [89]Zr-radiochemistry under basic conditions with fully deprotonated oxalate ($C_2O_4^{2-}$) and hydroxamate anions. The corresponding reaction coordinate showing the relative change in solvated free energies is presented in Figure 2.

Figure 2. DFT calculated reaction coordinate showing changes in solvated free energy for the step-wise conversion of $[Zr(C_2O_4)_4]^{4-}$ into the Zr(MeAHA)$_4$ product under basic conditions. Note: the table inset shows the number of equivalent hydroxamate (row 1) and dibasic oxalate anions (row 2) required for stoichiometric equivalence, and the frontier molecular orbital energy

gap (Δ_{FMO} / eV; for calculations using the DGDZVP basis set) of the Zr-species. The numbers listed under each energy level refer to the relative change in G_{sol} / kJ mol^{-1} *versus* the starting materials calculated using the LANL2DZ (black) and DGDZVP (red) basis sets with the B3LYP XC functionals.

Scheme 2. DFT calculated protic equilibria and isomerisation reactions involving oxalic acid and MeAHA. These reactions were used in elucidating the potential role of an acid-mediated mechanism of ligand substitution (see Scheme 3 and Figure 3).[75]

Scheme 3. Reaction scheme showing the 12-step acid-mediated reaction pathway of $[Zr(C_2O_4)_4]^{4-}$ ligand substitution involving initial protonation of the Zr-bound oxalate ligand, $HC_2O_4^-$ dissociation and MeAHA anion coordination. The corresponding reaction coordinate showing the relative change in solvated free energies is presented in Figure 3.

Figure 3. DFT calculated reaction coordinate showing changes in solvated free energy for the step-wise conversion of $[Zr(C_2O_4)_4]^{4-}$ into the Zr(MeAHA)$_4$ product under acid-mediated conditions. Note: the table inset shows the number of equivalent hydroxamate (row 1), dibasic oxalate anions (row 2), MeAHA acid (row 3), and monobasic $HC_2O_4^-$ anions required for stoichiometric equivalence. The numbers listed under each energy level refer to the relative change in calculated solvated free energy *versus* the starting materials (ΔG_{sol} / kJ mol^{-1}) estimated using the LANL2DZ (black) and DGDZVP (red) basis sets and the B3LYP functionals.

Figure 4. Molecular orbital diagram of $[Zr(C_2O_4)_4]^{4-}$ (dodecahedral, D_{2d} symmetry). Note: The default orientation of the Cartesian axes is presented with the *z*-axis parallel to the principle axis of rotation and the *y*-axis oriented in the plane of the molecule. In this standard spectroscopic axes definition, the metal d orbitals transform as irreducible representations: B1 (*xy*), E(*xz*, *yz*), B2 (x^2-y^2) and A1 (z^2). Occupied orbitals are shown in black, virtual orbitals are shown in red. Doubly degenerate orbital levels (E symmetry) are presented as double thickness lines. Molecular orbital isosurfaces (set at 96% to 97% occupancy) are presented for selected orbitals with significant contribution from Zr ion d orbitals. Energy levels presented as short lines are ligand-based with metal d orbital no contribution.

Figure 5. Molecular orbital diagram of $Zr(MeAHA)_4$ (distorted dodecahedral, C_1 symmetry). Note: Due to the twisted geometry of the ligands, the Cartesian coordinates differ from the orientation presented in Figure 4. This lack of symmetry and twisted geometry leads to significant d orbital mixing. Occupied orbitals are shown in black, virtual orbitals are shown in red. Doubly degenerate orbital levels (E symmetry) are presented as double thickness lines. Molecular orbital isosurfaces (set at 96% to 97% occupancy) are presented for selected orbitals with significant contribution from Zr ion d orbitals. Energy levels presented as short lines are ligand-based with metal d orbital no contribution.

Table 1.

	Parameter [d]					
Basis set [a]	r(Zr-O2N1) / Å r(Zr-O4N2) / Å	r(Zr-O1C1) / Å r(Zr-O3C2) / Å	r(N1-C1) / Å	r(N1-CH$_3$) / Å	r(C1-CH$_3$) / Å r(C2-CH$_3$) / Å	RMSD / Å[b]
LANL2DZ	2.190 2.160	2.243 2.350	1.341	1.458	1.507 1.513	0.377
DGDZVP	2.198 2.171	2.272 2.347	1.328	1.450	1.512 1.514	0.287
CEP-4G	2.205 2.175	2.253 2.348	1.350	1.470	1.528 1.530	0.398
CEP-31G	2.205 2.175	2.253 2.348	1.351	1.471	1.528 1.530	0.398
CEP-121G	2.208 2.176	2.251 2.345	1.346	1.466	1.522 1.523	0.386
SDDALL	2.210 2.178	2.238 2.341	1.331	1.456	1.501 1.505	0.387
LANL2DZ/6-31+G(d)	2.190 2.164	2.261 2.334	1.328	1.447	1.511 1.512	0.292
Sapporo-DZP/6-31+G(d)	2.185 2.157	2.262 2.339	1.328	1.447	1.512 1.513	0.286
Sapporo-TZP/6-31+G(d)	2.165 2.174	2.232 2.220	1.324	1.449	1.507 1.507	0.282
Experimental XRD [c]	2.228 2.140 2.203 2.196	2.194 2.182 2.195 2.206	1.316 1.284 1.260 1.333	1.509 1.464 1.485 1.494	1.487 1.445 1.445 1.505	-

[a] Calculated using the B3LYP exchange-correlation functional. [b] Root-mean-squared displacement weighted by the atomic mass of heavy atoms (i.e. excluding hydrogen atoms). [c] Experimental single-crystal X-ray data from Cambridge Crystallography Data Centre accession number 902586.[15] [d] Note that the calculations based on an input coordinates from the experimental single-crystal X-ray geometry revealed asymmetry in the optimised structures of

Zr(MeAHA)$_4$ consistent with two distinct ligand environments. MeAHA ligands *trans* to each other were found to be equivalent.

Table 2.

XC functionals [a]	Parameter					
	$r(\text{Zr-}\underline{\text{O2}}\text{N1})$ / Å $r(\text{Zr-}\underline{\text{O4}}\text{N2})$ / Å	$r(\text{Zr-}\underline{\text{O1}}\text{C1})$ / Å $r(\text{Zr-}\underline{\text{O3}}\text{C2})$ / Å	$r(\text{N1-C1})$ / Å	$r(\text{N1-CH}_3)$ / Å	$r(\text{C1-CH}_3)$ / Å $r(\text{C2-CH}_3)$ / Å	RMSD / Å
Pure-GGA functionals						
BLYP	2.223 2.208	2.300 2.342	1.343	1.464	1.524 1.525	0.243
BP86	2.209 2.194	2.278 2.317	1.339	1.455	1.516 1.517	0.235
BPW91	2.211 2.195	2.282 2.321	1.340	1.453	1.515 1.516	0.236
PW91PW91	2.207 2.188	2.273 2.318	1.338	1.450	1.512 1.513	0.233
BPBE	2.210 2.194	2.281 2.319	1.340	1.453	1.515 1.515	0.236
PBEPBE	2.210 2.192	2.277 2.319	1.339	1.451	1.513 1.514	0.231
PBELYP	2.223 2.205	2.296 2.343	1.344	1.461	1.522 1.523	0.242
G96LYP	2.217 2.203	2.295 2.335	1.343	1.460	1.523 1.523	0.244
mPWPW91	2.209 2.193	2.279 2.319	1.339	1.452	1.514 1.514	0.234
Hybrid-GGA functionals						
B1LYP	2.197 2.170	2.272 2.349	1.327	1.449	1.513 1.514	0.292
B3LYP	2.198 2.171	2.272 2.347	1.328	1.450	1.512 1.514	0.287
B3P86	2.184 2.158	2.251 2.321	1.324	1.440	1.504 1.505	0.281
B3PW91	2.189 2.163	2.259 2.329	1.325	1.443	1.506 1.507	0.275
BHandH	2.125 2.150	2.281 2.209	1.303	1.422	1.487 1.488	0.315

B97-1	2.193 / 2.168	2.271 / 2.349	1.329	1.448	1.515 / 1.516	0.282
B97-2	2.189 / 2.162	2.265 / 2.336	1.324	1.442	1.506 / 1.507	0.270
B98	2.190 / 2.165	2.268 / 2.347	1.328	1.448	1.515 / 1.516	0.283
O3LYP	2.200 / 2.180	2.285 / 2.335	1.330	1.446	1.510 / 1.510	0.240
X3LYP	2.196 / 2.169	2.268 / 2.344	1.327	1.448	1.511 / 1.512	0.289
PBE1PBE (PBE0)	2.184 / 2.157	2.252 / 2.323	1.322	1.439	1.503 / 1.504	0.279
THCTHH	2.191 / 2.165	2.261 / 2.334	1.329	1.447	1.513 / 1.514	0.278
mPW3LYP	2.197 / 2.170	2.269 / 2.344	1.328	1.448	1.512 / 1.513	0.286
MPW1N	2.171 / 2.145	2.242 / 2.316	1.313	1.433	1.497 / 1.498	0.293
Pure meta-GGA functionals						
BB95	2.207 / 2.183	2.269 / 2.339	1.339	1.452	1.513 / 1.514	0.286
BTPSS	2.212 / 2.197	2.285 / 2.323	1.340	1.453	1.515 / 1.515	0.236
TPSSTPSS	2.202 / 2.182	2.267 / 2.316	1.336	1.456	1.516 / 1.516	0.242
VSXC	2.198 / 2.174	2.282 / 2.327	1.337	1.454	1.504 / 1.508	0.747
Hybrid meta-GGA functionals						
TPSS1KCIS	2.173 / 2.148	2.244 / 2.317	1.311	1.434	1.497 / 1.498	0.297
BMK	2.185 / 2.165	2.267 / 2.336	1.321	1.442	1.519 / 1.520	0.310

[a] Calculated using the DGDZVP basis set.

$$[^{89}Zr(C_2O_4)_4]^{4-} \qquad ^{89}Zr(MeAHA)_4$$
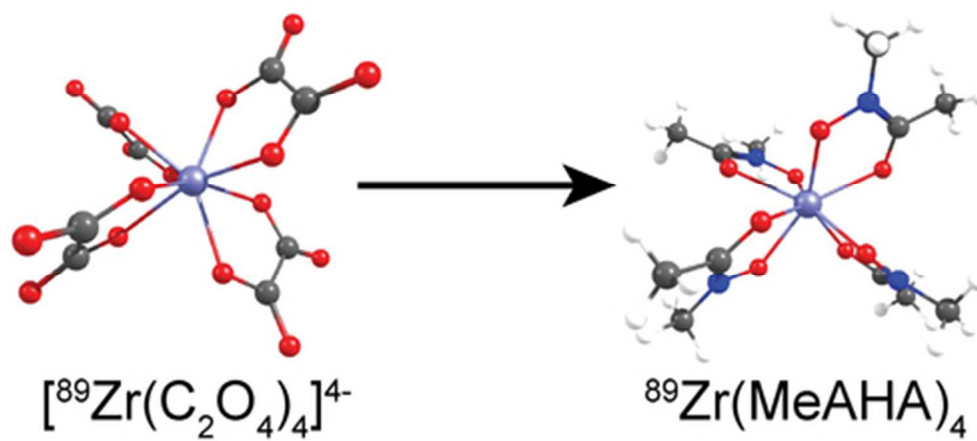
Graphical Abstract
41x19mm (300 x 300 DPI)
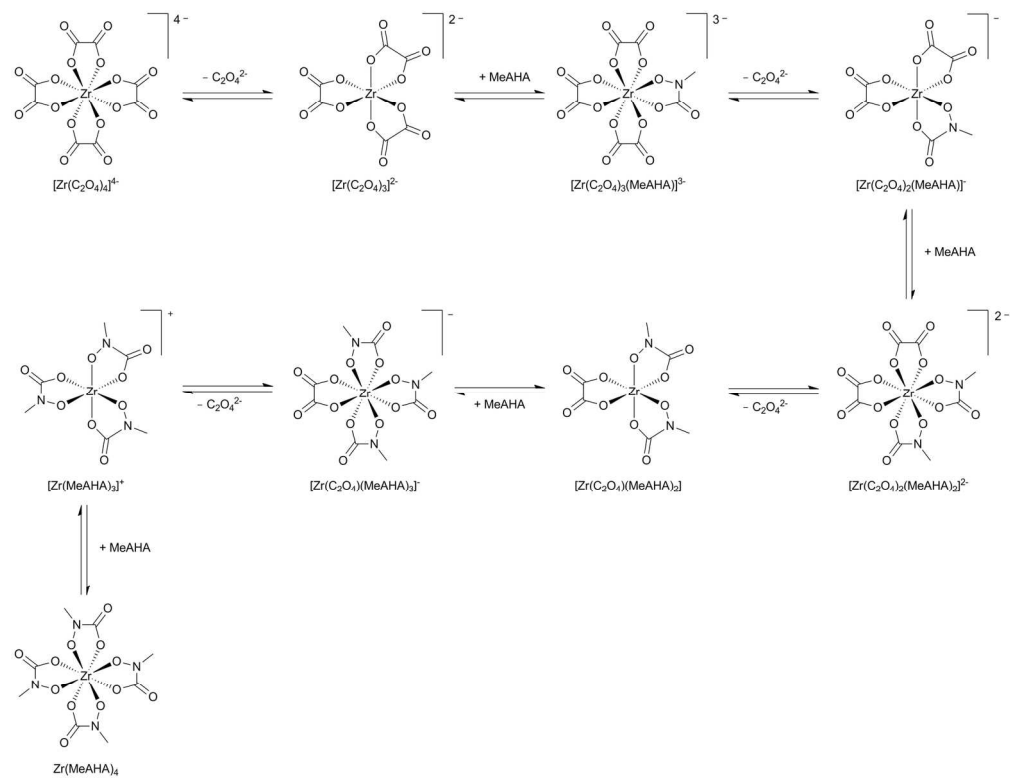
Scheme 1
160x124mm (300 x 300 DPI)
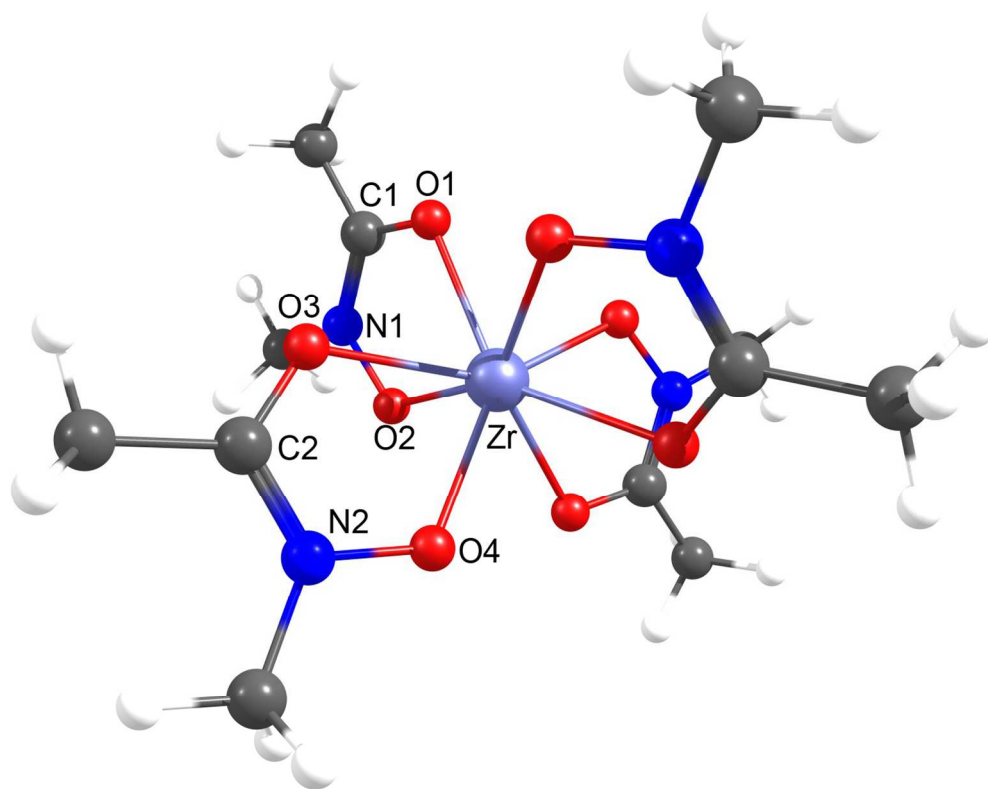
Figure 1
522x416mm (72 x 72 DPI)
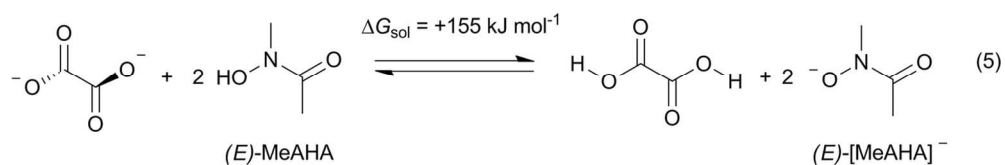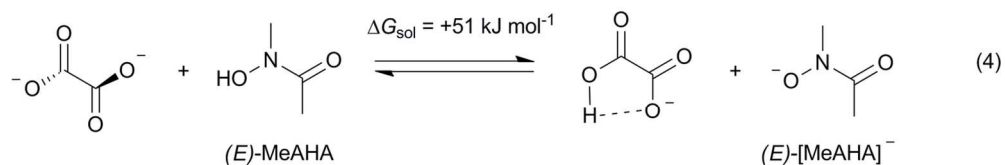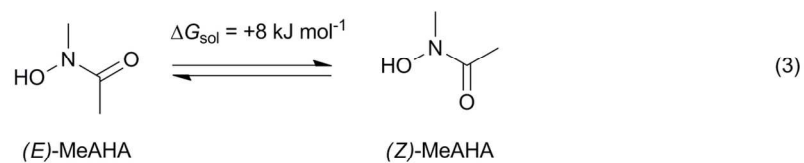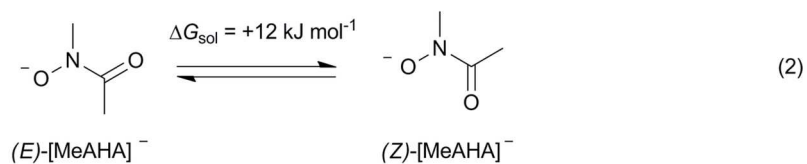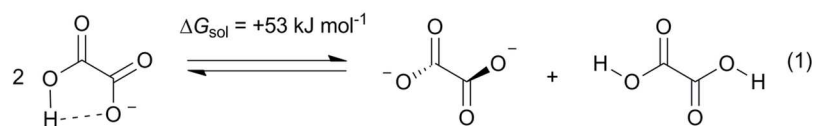
Scheme 2
128x141mm (300 x 300 DPI)

Scheme 3
226x255mm (300 x 300 DPI)
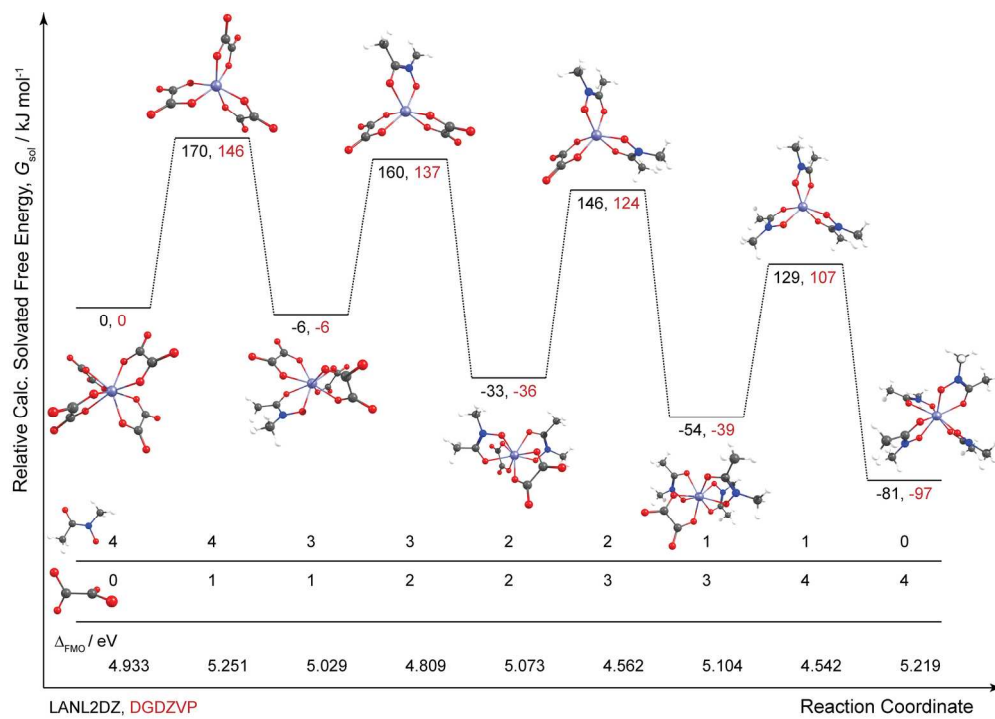
Figure 2
183x129mm (300 x 300 DPI)
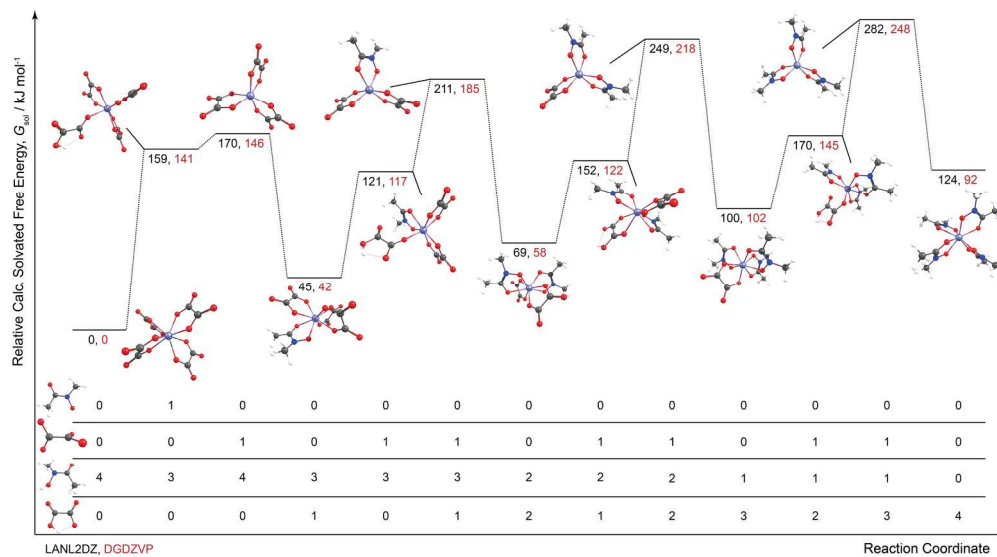
Figure 3
195x106mm (300 x 300 DPI)
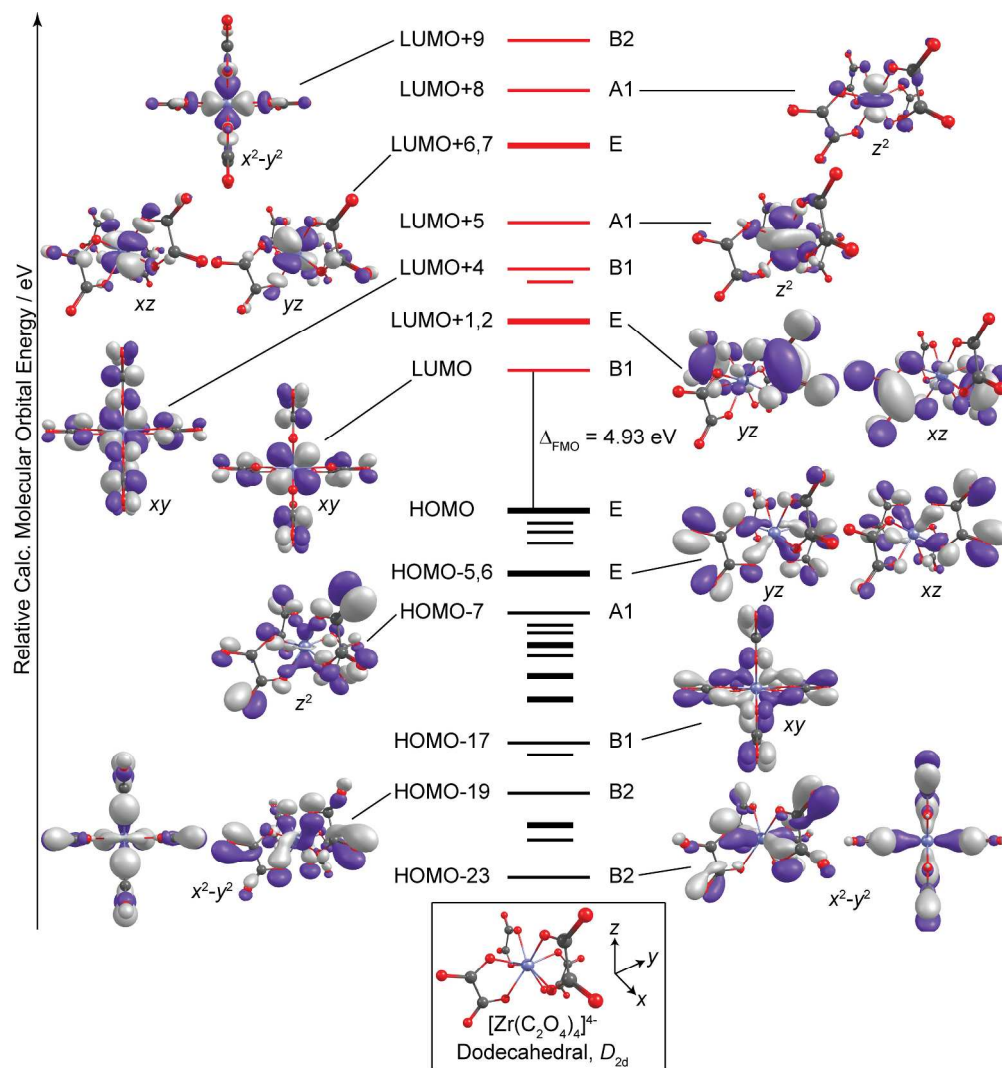
Figure 4
248x263mm (300 x 300 DPI)
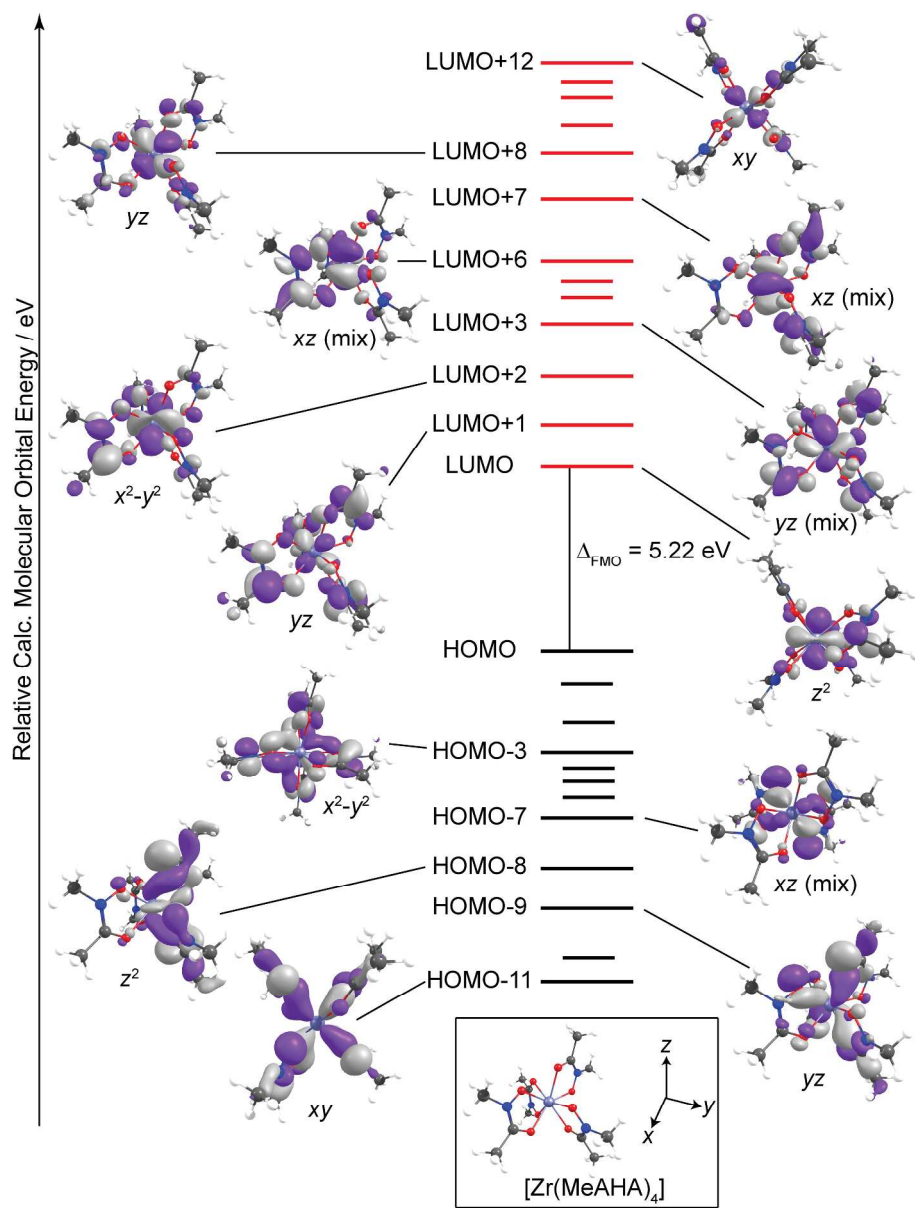
Figure 5
249x326mm (300 x 300 DPI)